

THE ROLE OF VELOCITY REDISTRIBUTION IN ENHANCING THE INTENSITY OF THE He II 304 Å LINE IN THE QUIET-SUN SPECTRUM

VINCENZO ANDRETTA,^{1,2} STUART D. JORDAN, JEFFREY W. BROSIUS,³ JOSEPH M. DAVILA, ROGER J. THOMAS,
 WILLIAM E. BEHRING, AND WILLIAM T. THOMPSON⁴

Laboratory for Astronomy and Solar Physics, NASA Goddard Space Flight Center, Code 682, Greenbelt, MD 20771

AND

ADRIANA GARCIA

Observatório Astronómico da Universidade de Coimbra, Santa Clara, 3040 Coimbra, Portugal

Received 1999 September 10; accepted 1999 December 21

ABSTRACT

We present observational evidence of the effect of small-scale (“microturbulent”) velocities in enhancing the intensity of the He II λ 304 line with respect to other transition region emission lines, a process we call “velocity redistribution.” We first show results from the 1991 and 1993 flights of SERTS (Solar EUV Rocket Telescope and Spectrograph). The spectral resolution of the SERTS instrument was sufficient to infer that, at the spatial resolution of 5”, the line profile is nearly Gaussian both in the quiet Sun and in active regions. We were then able to determine, for the quiet Sun, a lower limit for the amplitude of nonthermal motions in the region of formation of the 304 Å line of the order of 10 km s^{−1}. We estimated that, in the presence of the steep temperature gradients of the solar transition region (TR), velocities of this magnitude can significantly enhance the intensity of that line, thus at least helping to bridge the gap between calculated and observed values. We also estimated the functional dependence of such an enhancement on the relevant parameters (nonthermal velocities, temperature gradient, and pressure). We then present results from a coordinated campaign, using *SOHO*/CDS and H α spectroheliograms from Coimbra Observatory, aimed at determining the relationship between regions of enhanced helium emission and chromospheric velocity fields and transition region emission in the quiescent atmosphere. Using these data, we examined the behavior of the He II λ 304 line in the quiet-Sun supergranular network and compared it with other TR lines, in particular with O III λ 600. We also examined the association of 304 Å emission with the so-called coarse dark mottle, chromospheric structures seen in H α red-wing images and associated with spicules. We found that all these observations are consistent with the velocity redistribution picture.

Subject headings: line: formation — line: profiles — Sun: atmospheric motions — Sun: chromosphere — Sun: corona — Sun: transition region

1. INTRODUCTION

A recent study with *SOHO* observations (Macpherson & Jordan 1999, henceforth MJ99) has confirmed an earlier result of the *Skylab* era, that the observed intensities in the principal resonance line of He II, the 304 Å line, exceed in the quiet Sun by a factor of 3, and possibly even by an order of magnitude or more, the values computed from empirical model solar atmospheres that reproduce the other strong transition region (TR) line intensities very well. A number of suggestions have been offered to explain this situation. One of the earliest proposals, developed to describe visible and EUV (extreme ultraviolet) observations predating *Skylab*, invokes the so-called photoionization-recombination (P-R) mechanism. According to that model, the He II λ 304 radiation, in fact the entire solar helium spectrum, is due to recombination cascades following ionization by EUV coronal radiation impinging on the chromosphere (photoionization thresholds: 504 Å for He⁰, and 228 Å for He⁺). A standard discussion of this process can be found in Zirin (1988), p. 198. This process has often been regarded as

the “natural” solution to the problem of the anomalous intensities of helium lines; but careful analyses of the observations have revealed some inconsistencies, especially in the quiet Sun (e.g., Milkey 1975; Athay 1988; Kohl 1977; Jordan et al. 1993; Andretta & Jones 1997).

Alternatively, Shine, Gerola, & Linsky (1975) suggested that diffusion of He⁺ ions into a region of higher temperature thermal electrons could provide the enhancement mechanism, in the case of collision-stimulated 304 Å radiation. However, calculations by Fontenla, Avrett, & Loeser (1993) showed that diffusion (namely, ambipolar diffusion) had only a small effect on the He⁺ ions, though it had a large effect on hydrogen atoms and protons (yielding hydrogen Ly α profiles that compared well with observations without the artificial “temperature plateau” previously invoked for that purpose, giving the Fontenla et al. study considerable credibility). Recent preliminary calculations by Avrett (1999) include the effect of flows as well and thus put these results on a firmer basis. However, it is still unclear to what extent the combined effect of diffusion and flows in average, time-independent models can account for the observed discrepancies.

Another possibility was proposed by C. Jordan (1975, 1980, henceforth: CJ75, CJ80, respectively), who noted that, if the 304 Å line were collision dominated, as a growing body of evidence suggests, the extreme sensitivity of its collision source term to increases in electron temperature,

¹ Also: Physics Department, Catholic University of America, Washington, DC.

² Present address: Osservatorio Astronomico di Capodimonte, Via Moirariello, 16, 80131 Napoli, Italy; andretta@na.astro.it.

³ Raytheon ITSS.

⁴ SM&A Corporation, Space Science and Engineering Division.

compared to the other strong collision-dominated lines in the TR, meant that exposure to higher temperature electrons by *any* mechanism would produce a differential intensity enhancement in He II $\lambda 304$. For instance, microturbulent or larger scale movement of He⁺ ions into a region of higher temperature thermal electrons could produce the observed intensity enhancement, given the more rapid thermalization of the moving “blobs” compared to the time for collisional excitation in the line. On the other hand, any mechanism that would create and sustain “higher temperature” electrons in situ could do the job as well. Since Jordan’s suggestion appeared, both means of intensity enhancement have been proposed and investigated.

The latter possibility, in situ production of nonthermal, “hot” electrons in the transition region, is a requisite of the so-called velocity filtration mechanism for coronal heating, proposed by Scudder (1992a, 1992b) and evaluated by Anderson (1994), Anderson, Raymond, & van Ballegooijen (1996), and, more recently, by Viñas, Wong, & Klimas (2000). Anderson et al. found it difficult to reconcile the observed intensities of all the strong TR and coronal lines in a temperature structure determined by collisionless “filtration” of the nonthermal electrons in the solar gravitational field. On the other hand, Viñas has proposed a plasma instability for driving the electron distribution function away from Maxwellian in the high-energy tail, arguing that this process could produce a sustainable distribution because it operates at a sufficiently high frequency to overcome damping by the background electrons. Thus, at this stage, we believe that this mechanism must be regarded as a candidate for at least contributing to the 304 Å intensity enhancement. However, much work still needs to be done to assess whether the conditions for this process to be effective are realistically present in the solar atmosphere.

The other suggestion offered by CJ75, CJ80, a velocity redistribution of the He⁺ ions, is the subject of this paper. A preliminary study of SERTS spectra supported this suggestion (Jordan 1994). We now present much more extensive evidence, based on observations taken with the SERTS sounding rocket in 1991 and 1993 and supplemented by more recent *SOHO* and ground-based results, that a redistribution of the He⁺ ions by comparatively small-scale “microturbulent” motions in the presence of a sharp TR temperature gradient makes a significant contribution to the required intensity enhancement in the quiet Sun. Further support for this hypothesis, which we have chosen to call “velocity redistribution,” is provided by an analysis based on an earlier SERTS flight in 1989, that makes a strong case for collision domination of the 304 Å line, at least in the quiet Sun and possibly in active regions as well (Jordan et al. 1993), an effect that is confirmed by results from a recent SERTS flight, in 1997, reported later in this paper.

The paper is organized as follows. In § 2 we present and analyze SERTS observations of the He II $\lambda 304$ line from the 1991 and 1993 flights. In § 2.1 we review the “velocity redistribution” mechanism and show that substantial unresolved motions (a requisite of that mechanism) are present in the region of formation of the 304 Å line, at least in the quiet Sun. Having established the plausibility of a significant role of the “velocity redistribution” mechanism in the quiet Sun, in § 3 we discuss the 1998 June 20–21 coordinated H α and *SOHO* observations, investigating the

relationship between the 304 Å line and quiet-Sun chromospheric and TR structures.

2. SERTS OBSERVATIONS

The SERTS observations used for this study include spectra and images in the He II $\lambda 304$ line taken during the 1991 May 7 and the 1993 August 17 flights, denoted in this paper as SERTS-91 and SERTS-93, respectively. The science instrumentation was identical on the two flights, making the two sets of observations highly compatible. A basic description of the instrument is given in Neupert et al. (1992). The unique “dumbbell” shape of the SERTS entrance slit permitted us to obtain spectra of both active regions and quiet Sun, over areas that were also imaged in the same wavelengths in near-real time. The spectral resolution for these flights was approximately 55 mÅ (FWHM, see below), and the spatial resolution about 5". Further details on the configuration of the SERTS instrument, as well as an analysis of average active-region and quiet-Sun spectra for the above two flights are given in Brosius et al. (1996).

Slit spectra were selected from two different pointing positions during each flight. For SERTS-91, the second pointing position yielded narrow-slit spectra over the edge of active region NOAA 6615 (S08, W32) and images (spectroheliograms) of the quiet Sun in the lower wide lobe that crossed the west limb, as shown in the left-hand panel of Figure 1. We will refer to this pointing position as SERTS-91 position A. At the first pointing position, the upper wide lobe imaged the same active region while the narrow slit provided spectra of the previously imaged adjacent area that was partially off the limb (SERTS-91 position Q). For SERTS-93, the slit at the first pointing position bisected active region NOAA 7563 (S01, W15) and will be referred to as SERTS-93 position A (right-hand panel of Fig. 1). For the second pointing position, the narrow slit was moved over a prevalently quiescent area (SERTS-93 position Q), while the wide-slit provided imaging of the active region. We selected the best 64 spatially resolved spectra along the narrow slit in all the cases.

Positions A on both SERTS-91 and SERTS-93 yield a mixture of quiet-Sun and active-region spectra. In contrast, SERTS-93 position Q gives quiet-Sun spectra only, while SERTS-91 position Q yields only quiet-Sun spectra inside the limb and other off-limb spectra not used for this analysis. Using the criteria discussed in Brosius et al. (1996), and after excluding the off-limb spectra of SERTS-91 position Q, these data gave a total of 87 spectra of active-region intensities (36 and 51 from SERTS-91 and SERTS-93, respectively) and 169 quiet-Sun spectra (92 and 77). Because of their proximity to the limb, we also excluded from the line width analysis of § 2.1.2 the remaining 30 on-disk spectra of SERTS-91 position Q.

The SERTS spectral resolution enabled us to separate the He II $\lambda 304$ line from the nearby Si XI $\lambda 303$ line. Figure 2 shows representative He II $\lambda 304$ profiles observed in active and quiet regions, together with their Gaussian fits. Since the line intensity in active regions is much higher than in quiet Sun, we show in this figure normalized intensities only, in order to display more clearly similarities and differences between the two profiles. In particular, both profiles appear to be very nearly Gaussian. In fact, we found that none of the SERTS-91 or -93 He II $\lambda 304$ spectra seems to show any hint of a central reversal or any large departures

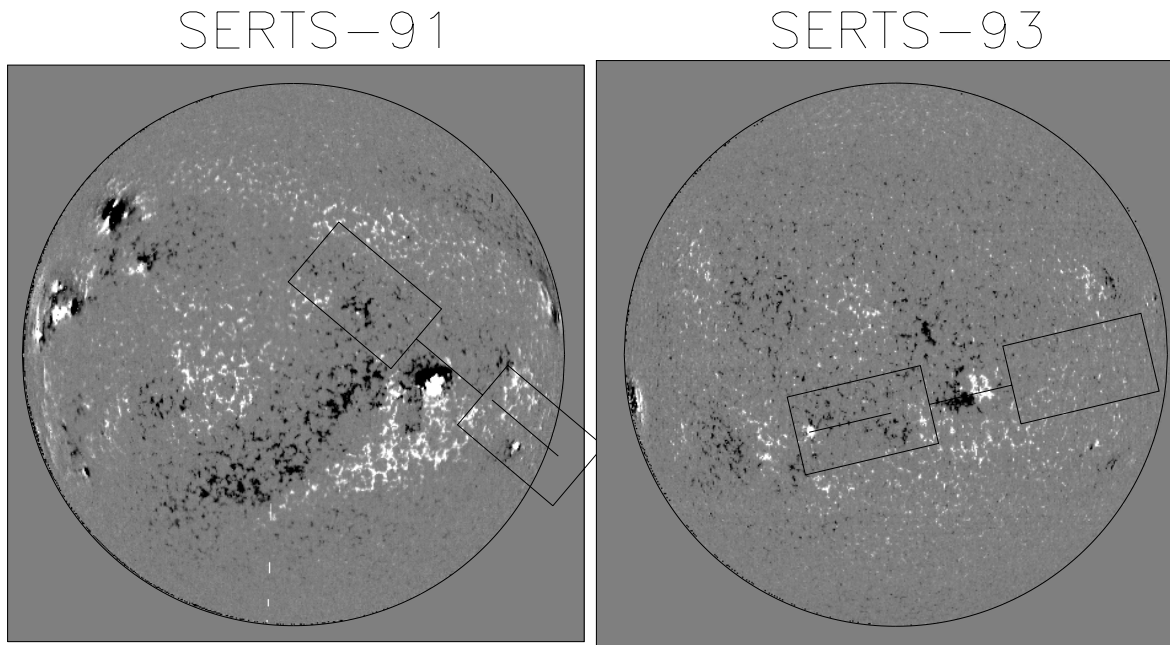


FIG. 1.—Pointing positions during SERTS-91 (1991 May 7, position A; left-hand panel) and SERTS-93 (1993 August 17, position A; right-hand panel). The location of the narrow slit in positions Q of both flights is indicated by a solid line within one of the two wide lobes. In each image north is at the top.

from a Gaussian profile. On the other hand, Milkey (1975) showed that the P-R process should produce a strong central reversal in the profile of this line. The absence of this feature in our observed profiles offers further support for collisional excitation.

The SERTS data analyzed consisted of EUV intensities observed at each spatial and spectral pixel. Over a range of 25 spectral pixels, approximately centered on the 304 Å line, for each spatial position along the narrow slit the spectra were then fitted by a single Gaussian fitting routine. The routine used removed the adjacent continuum using a linear fit to the continuum, which contained no other significant lines over this spectral range. From this fitting of the nearly

Gaussian profiles observed, we obtained values for the total line intensity, the measured width, σ_M , and the line-center position on the wavelength axis, λ_0 , and their errors, using the following definition for the normalized Gaussian profile:

$$\varphi(\lambda) = \frac{1}{\sqrt{2\pi}\sigma_M} \exp \left[-\frac{1}{2} \left(\frac{\lambda - \lambda_0}{\sigma_M} \right)^2 \right]. \quad (1)$$

We assumed that the thermal width of the line is the value given by the temperature at which the contribution to the emission in He II $\lambda 304$ reaches its maximum. CJ75 estimates that temperature to be 80,000 K, in the optically thin case. We obtained approximately the same value by using more recent atomic data (see § 2.1.1), and the same differential emission measure (DEM) distribution given in that paper. We obtained slightly lower values, about 75,000 and 70,000 K, when using the DEMs given by Dere & Mason (1993) or by Raymond & Doyle (1981), respectively. We note that, because of the steep temperature dependence of the relevant excitation rates, this temperature is substantially higher than the temperature of maximum fractional abundance of He⁺, estimated at $\approx 50,000$ K by using data from Arnaud & Rothenflug (1985). At the temperature $T = 80,000$ K, the thermal width of the He II $\lambda 304$ line is

$$\sigma_T = \frac{\lambda}{c} \sqrt{\frac{kT}{M_{\text{He}}}} = 13.06 \text{ mÅ}, \quad (2)$$

where M_{He} is the mass of the helium nucleus and λ is the wavelength of the line.

The SERTS instrumental width, σ_I (same value for both flights), was measured in the laboratory and was found to vary slowly in the range ≈ 20 –26 mÅ and almost linearly along the slit. Its dependence on the slit position can be approximated by

$$\sigma_I = 11 \times [1.8445 + 0.0085 \times (n - 1)] \text{ mÅ}, \quad (3)$$

where n is the spatial pixel position in the range 1–64.

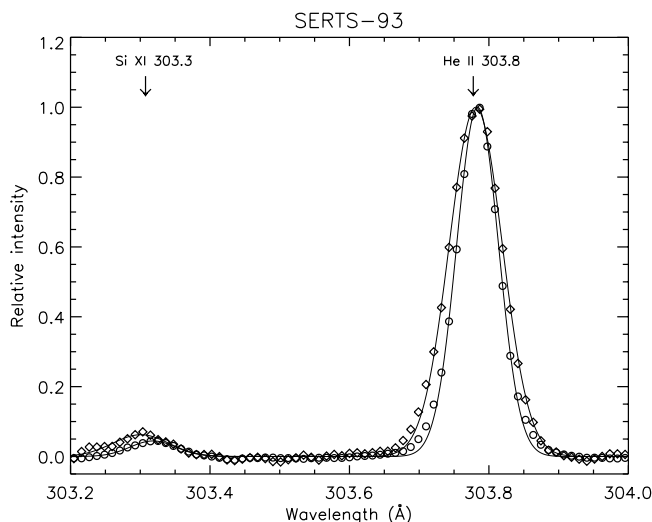


FIG. 2.—Representative profiles from SERTS-93, position A, averaged over 11 spatial pixels, to improve signal-to-noise ratio. Profiles are normalized to the peak intensity of the He II $\lambda 304$ line. Diamonds and circles represent profiles from the quiet Sun and active regions, respectively. The solid lines are Gaussian fits to the observed profiles.

Using the values for thermal line width and instrumental width given above, we then determined the residual, or “nonthermal,” line width,

$$\sigma_R = \sqrt{\sigma_M^2 - \sigma_I^2 - \sigma_T^2}, \quad (4)$$

expressed as a nonthermal velocity. In three SERTS-93 spectra, the observed widths were nearly equal to σ_I : for those points we set σ_R equal to zero.

From the line center positions, we also computed the relative Doppler velocity shifts from the nominal wavelength of the line (303.782 Å). Since the wavelength calibration is known only up to some overall constant offset, estimated to be of the order of 5 km s⁻¹, the absolute Doppler velocity shifts remain undetermined.

In Figure 3 we show the run of the fitted parameters (intensity, line shift, residual width) along the slit, for both SERTS-91 and -93. From Figures 2 and 3, it is readily apparent that line widths are smaller in those regions where line intensities are higher. In fact, as we will show in § 2.1.2, we consistently obtained an anticorrelation between intensity and residual line width. This behavior is in contrast with what is expected from opacity effects, and it is also the opposite of what is observed in other probably optically thick TR lines, such as the C IV $\lambda\lambda 1548, 1550$ and Si IV $\lambda\lambda 1393, 1402$ doublets (Dere & Mason 1993).

2.1. Interpretation of the SERTS Observations

The anticorrelation observed between intensity and residual line width in the SERTS-91 and -93 data suggests that the actual small-scale velocities of the emitting ions may be greater in the quieter radiating elements than in and

near the active regions observed. If this is true, then the mechanism of velocity redistribution could contribute significantly to the intensity enhancement of the He II $\lambda 304$ line in the quiet Sun. In order to show that this situation is plausible, we do two things in this section. First, we review the results of a simple calculation that shows the effect of an isotropic microturbulent velocity field in the TR of velocity amplitude V_{NT} in enhancing the emission of the 304 Å line in the presence of different TR temperature gradients and physical conditions in the lower TR. The method employed follows closely the plausibility argument given by CJ80. The TR parameters fall in a range given by numerous extant TR models for quiet Sun and active-region conditions.

We next develop a simple procedure for establishing a reasonable lower limit on the actual small-scale nonthermal velocities of the emitting ions, in the quiet Sun. This method takes into account the fact that the 304 Å line is most likely optically thick, even in the quiet Sun. It is also assumed that the temperature at which these photons are produced—at which collisional excitation in the line occurs—is not sufficiently greater in the quiet Sun than it is in the active region for thermal effects to “fill in” the differences in line width. We thus find that the magnitude of these nonthermal velocities in the quiet Sun is comparable with observations from other, optically thin TR lines and compatible with a significant enhancement of the line intensity.

2.1.1. Estimation of the “Velocity Redistribution” Effect

To illustrate the velocity redistribution effect for a range of physical conditions we can expect to actually encounter in the lower solar TR, we follow the approach of CJ80.

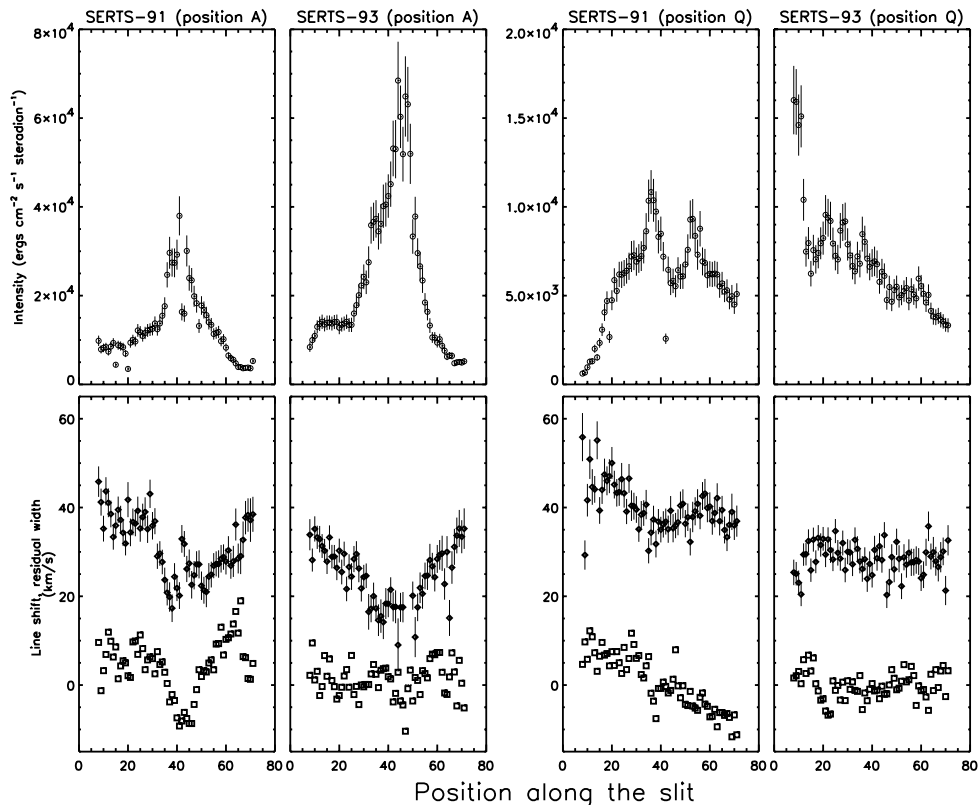


FIG. 3.—Fitted parameters (intensity, shift, residual width) as function of slit position for both pointing positions A (left-hand panels) and Q (right-hand panels) of SERTS-91 and SERTS-93. In the lower panels, line shifts are marked by squares (with positive values representing blueshifts), residual widths by diamonds. For the SERTS-93 spectra, the first slit position corresponds to the easternmost part of the slit; for SERTS-91 spectra, the first slit position is near or off the limb (see Fig. 1). Errors for the line shifts are not marked because of the uncertainty in the wavelength calibration.

Elaborating somewhat on that simple picture permits us to estimate intensity enhancements as a function of a range of TR conditions found in both quiet and active emitting elements.

Invoking the assumption of electron collisional excitation from the ground state (level L) to levels with principal quantum number $n = 2$ (level U), we can write the collision time for excitation in terms of collisional excitation rate, C_{LU} :

$$t_{\text{exc}} = 1/C_{LU} . \quad (5)$$

In turn, the collisional excitation rate can be written as

$$\begin{aligned} C_{LU} &= N_e 8.63 \times 10^{-6} T_e^{-1/2} [\Omega(T_e)/g_L] \exp(-\chi_{LU}/kT_e) \\ &= N_e q_{LU}(T_e) , \end{aligned} \quad (6)$$

where χ_{LU} is the excitation energy of the transition, g_L is the degeneracy of the ground state, and Ω_{LU} is the effective (thermally averaged) collision strength; all other symbols have their usual meaning. We adopted the calculated values for $\Omega_{LU}(T_e)$ from Aggarwal et al. (1992).

If we consider a “blob” of plasma containing He^+ ions in a “microturbulent” velocity field of mean absolute amplitude V_{NT} , the distance traveled by such plasma element before the upper level of the $\text{He II } \lambda 304$ line is excited is then

$$\Delta h = V_{\text{NT}} t_{\text{exc}} = V_{\text{NT}}/C_{LU} . \quad (7)$$

In presence of a temperature gradient of magnitude ∇T_e , such a distance corresponds to a temperature difference:

$$T_{ef}^{\pm} - T_{ei} = \pm \nabla T_e \Delta h , \quad (8)$$

where T_{ei} and T_{ef}^{\pm} are the initial and final (or “emission”) temperatures, respectively, to which the plasma element is exposed, and the positive (negative) sign applies to ions moving toward higher (lower) temperatures. We will omit the sign in the symbol of T_{ef} when we do not need to differentiate between the two cases.

For a plasma element moving along the temperature gradient toward higher temperatures (“upward”), the relevant (shortest) excitation time is set by the excitation rate at T_{ef} . Thus, combining the above expressions (5)–(8), we can implicitly define T_{ef} in terms of T_{ei} :

$$\begin{aligned} T_{ef}^+ &= T_{ei} + \left(\frac{V_{\text{NT}} \nabla T_e}{P_e} \right) \left[\frac{T_{ef}^+}{q_{LU}(T_{ef}^+)} \right] \\ &= T_{ei} + M \left[\frac{T_{ef}^+}{q_{LU}(T_{ef}^+)} \right] . \end{aligned} \quad (9)$$

The parameter in the rightmost term of equation (9),

$$M = \frac{V_{\text{NT}} \nabla T_e}{P_e} \quad (10)$$

(which we may call “velocity redistribution parameter”), encloses the dependence of T_{ef} upon the physical conditions of the atmosphere (for simplicity, we have made the further assumption of constant electron pressure: $P_e = P_{ef} = P_{ei} = N_{ei} T_{ei}$).

Similarly, for a plasma element moving toward lower temperatures (“downward”), the shortest excitation time is set by the rate at T_{ei} , and therefore

$$T_{ef}^- = T_{ei} - M \left[\frac{T_{ei}}{q_{LU}(T_{ei})} \right] . \quad (11)$$

This illustrative one-dimensional model shows that the temperature T_{ef} at which emission occurs is determined by the initial conditions of the small-scale “blob,” (P_{ei} , T_{ei}), the temperature gradient in the direction of motion, ∇T_e , and the mean “microturbulent” velocity at which this blob moves, V_{NT} , through the velocity redistribution parameter M defined by equation (10):

$$T_{ef}^{\pm} = \mathcal{F}(T_{ei}, \pm M) . \quad (12)$$

In order to estimate the relative photon production rate between the “standard” case, $M = 0$ (i.e., $V_{\text{NT}} = 0$, and/or $\nabla T_e = 0$, and/or $P_e \rightarrow \infty$) and the case of nonzero M , we can assume that the ion population in the plasma “blob” remains the same (an approximation applicable if the relevant ionization and recombination times are much longer than t_{exc}). Then the enhancement factor is simply the ratio of the rates from equation (6) under the different physical conditions in the two cases:

$$Y_f^{\pm} \equiv \frac{I_f^{\pm}(\text{He II } \lambda 304)}{I_i(\text{He II } \lambda 304)} = \frac{C_{LU}(P_{ef}, T_{ef}^{\pm})}{C_{LU}(P_{ei}, T_{ei})} = \mathcal{H}(T_{ei}, \pm M) , \quad (13)$$

where in the last passage we have once more used the approximation of constant TR pressure and applied equation (12) to eliminate T_{ef} .

For values of M approaching or exceeding $q_{LU}(T_{ei})$, equation (11) does not provide meaningful estimates of T_{ef}^- . In this case, because of the strong temperature dependence of the $\exp(-\chi_{LU}/kT_e)$ term in the collisional rate, we can however assume that T_{ef}^- is much smaller than T_{ei} , and therefore that $Y_f^- \approx 0$. If we make the latter approximation for all values of M , and assume an isotropic velocity field where about half the He^+ ions move “upward,” we obtain a conservative enhancement for the intensity enhancement:

$$Y_f^u \approx \frac{1}{2} Y_f^+ = \frac{1}{2} \mathcal{H}(T_{ei}, +M) . \quad (14)$$

This estimate of the enhancement factor is essentially the same as in equation (15) of CJ80, except for the conservative factor $\frac{1}{2}$.

The above approach can be generalized by considering an ensemble of plasma elements in a “microturbulent” velocity field whose statistical distribution is determined by a Gaussian with standard deviation V_{NT} : $G(V) = \exp[-(V/V_{\text{NT}})^2/2]/(\sqrt{2\pi}V_{\text{NT}})$. As in the customary treatment of microturbulent broadening of optically thin lines, the line intensity profile is obtained by convolving the above distribution with the “intrinsic” profile, $I_f \phi_{\lambda}$, which includes thermal and possibly other types of broadening in the rest frame of each plasma element. However, the intrinsic profile now depends on the velocity V not only via the Doppler-shifted wavelength λ but also via the enhancement factor and the velocity redistribution parameter: $I_f(V) = I_i \mathcal{H}[M(V)]$ (eq. [13]). It is easy to see that this is equivalent to convolving the line profile in the case $V = 0$ (i.e., $I_i \phi_{\lambda}$) with the distribution $\Phi(T_{ei}, V) = G(V) \mathcal{H}(T_{ei}, MV/V_{\text{NT}})$, where we have retained the definition of M in terms of V_{NT} , as in equation (10). The total enhancement factor relative to I_i is then

$$Y_f = \int \Phi(T_{ei}, V) dV = \mathcal{G}(T_{ei}, M) . \quad (15)$$

It is important to realize that the estimate of the intensity enhancement resulting from the application of this equation

is still conservative because we are treating the unrealistic, optically thin case, in which half the photons emitted are lost to the lower solar atmosphere. The photon enhancement from the actual optically thick atmosphere would be greater, as most of the photons created would be scattered out of the atmosphere in the observed line.

The product of this analysis is the emission temperature and intensity enhancement for the individual plasma blob, T_{ef}^\pm (eq. [12]) and Y_f^\pm (eq. [13]) respectively, and the total enhancement in a microturbulent velocity field, Y_f (eq. [15]), as functions of the atmospheric parameter M and of the initial electron temperature, T_{ei} . The initial electron temperature, T_{ei} , is chosen to be that value at which the emissivity of the He II $\lambda 304$ line peaks, in equilibrium conditions (viz. $T_{ei} = T_{ef}$). As noted earlier, this value is approximately 80,000 K. The resulting enhancement curves are shown in the upper panel of Figure 4.

In the same figure, we also show the enhancement factors computed for $T_{ei} = 70,000$ K. This demonstrates that the enhancement factors are quite sensitive to the choice of the initial temperature. In what follows, we will continue to assume that $T_{ei} = 80,000$ K, but bearing in mind that quantitative results (in particular, how steep is the dependence of

Y_f on M ?) depend critically on this choice. In particular, if T_{ei} is to be taken as the temperature of the peak of the line emissivity, its value will depend on the shape of the DEM curve, as discussed at the beginning of § 2.

Furthermore, Figure 4 shows that over a broad range of the parameter M , the enhancement factor Y_f can be approximated with a power law of index in the range 0.4–0.5. A better approximation for the enhancement factor can be estimated in the form

$$Y_f(m) \approx 1 + am^be^{-c/m}, \quad (16)$$

where m is the nondimensional quantity $M/q_{LU}(T_{ei})$, while the best-fit coefficients are $a = 0.841$, $b = 0.505$, and $c = 0.93$ for $T_{ei} = 80,000$ K (where $q_{LU} = 2.58 \times 10^{-11} \text{ cm}^3 \text{ s}^{-1}$), and $a = 0.900$, $b = 0.593$, and $c = 0.65$ for $T_{ei} = 70,000$ K (where $q_{LU} = 1.17 \times 10^{-11} \text{ cm}^3 \text{ s}^{-1}$). The above approximation reproduces the numerical results of equation (15) within 2% for $M \leq 20 \times q_{LU}(T_{ei})$. Equation (16) also highlights the fact that the velocity redistribution mechanism is effective for $M \gtrsim q_{LU}(T_{ei})$, and thus its onset depends exponentially upon T_{ei} .

Once the electron pressure is specified, the function $Y_f(M) = \mathcal{G}(T_{ei}, M)$ can be translated into loci of constant enhancement factors (hyperbolas) in the plane $(V_{NT}, \nabla T_e)$ (eq. [10]). The results for $T_{ei} = 80,000$ K are shown in the lower panels of Figure 4, for TR electron pressures that can be considered representative of quiet-Sun and active-region conditions, respectively.

We see that for quiet-Sun conditions, a significant enhancement, up to a factor ≈ 5 , can be achieved by V_{NT} of the order of, say, 10 km s^{-1} or more and for TR gradients of the order of $(1-10) \times 10^6 \text{ K Mm}^{-1}$ (in the range of most existing quiet-Sun TR models), but that for thicker TRs the enhancement is too small for velocity redistribution to be significant even for relatively high velocities. Likewise, the same is true if too high a pressure is considered. The reason for this is that the excitation time, t_{exc} , decreases with density, reducing the distance traveled by the plasma blob before photon emission occurs (eqs. [5]–[7]).

On the other hand, MJ99 give estimates for the enhancement of the He II $\lambda 304$ line in the quiet Sun that are of the order of 10 or higher, with values up to 50 (25 if all the photons escape the atmosphere) in supergranular cell interiors. These values are beyond those that can be obtained with equation (15) for $T_{ei} = 80,000$ K, but again an additional factor $\lesssim 2$ could be gained from backscattering from the lower atmosphere; as pointed out earlier, higher values can also be obtained with $T_{ei} < 80,000$ K. Even higher enhancements could be obtained with a direct application of equation (13), as was done in the original formulation of CJ75, CJ80, but in this case it has to be assumed that all the plasma blobs move upward (i.e., eq. [14] without the factor $\frac{1}{2}$).

In § 3 we will show simultaneous observations of the He II $\lambda 304$ and O III $\lambda 600$ lines. For the latter line, we have verified that velocity distribution is not an effective enhancement mechanism, as postulated by CJ80 for typical (other than helium) TR lines. We followed the same approach delineated by equations (5)–(15), except that we included in the collisional rate (eq. [6]) excitation from the three levels $1s^2 2s^2 2p^2 \text{ } ^3\text{P}$, ^1D , and ^1S (the 600 Å line itself is produced by the transition $1s^2 2s^2 2p^3 \text{ } ^1\text{D} \rightarrow 1s^2 2s^2 2p^2 \text{ } ^1\text{D}$). Using the effective collision strengths from Aggarwal (1993) and the ionic fractions for O^{++} by Arnaud & Rothenflug (1985), we esti-

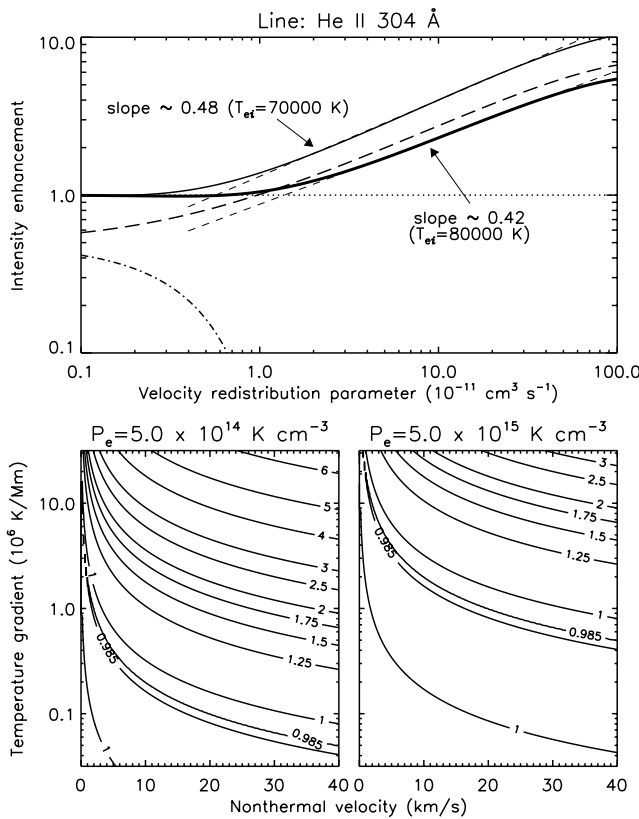


FIG. 4.—Upper panel: Dependence of the enhancement factor, Y_f , upon the velocity redistribution parameter, M , for $T_{ei} = 80,000$ K (solid, thick line). Enhancement factors calculated for $T_{ei} = 70,000$ K are shown with a thinner line. The limit value for $M \rightarrow 0$, $Y_f = 1$, is indicated with a horizontal dotted line. Power-law approximations of the function $Y_f(M)$ are shown with a thin-dashed line. Enhancements at $T_{ei} = 80,000$ K from upward- and downward-moving plasma blobs, times a conservative factor $\frac{1}{2}$, $Y_f^\pm/2$ (see also eq. [14]), are indicated by a long-dashed and dash-dotted line, respectively. Lower panels: Loci of constant enhancement factors, at $T_{ei} = 80,000$ K, as function of temperature gradient and nonthermal velocities, at two values of the electron pressure representative of the quiet Sun (lower left-hand panel) and active regions (lower right-hand panel).

mated that the line contribution function peaks around 10^5 K. Using this value as T_{ei} , we estimated that for the same range of values as in Figure 4, velocity distribution produces practically negligible enhancements of the line intensity.

2.1.2. Estimation of a Lower Limit on Actual Quiet-Sun Small-Scale Nonthermal Velocities

We have shown how nonthermal velocities of the order of 10 km s^{-1} or more in the steep gradient of the solar TR can effectively enhance the intensity of the He II line. We now want to estimate the actual magnitude of nonthermal velocities in the region of formation of the He II line. To do so, we use the fact that the line is broader in quiet Sun than in active areas and assume that the optical depth in the quiet-Sun profile is equal to, or smaller than, the optical depth in active regions.

In their interpretation of earlier He II $\lambda 304$ observations, Kastner & Bhatia (1998) assume, on the contrary, that the line observed in active regions is practically optically thin. Thus, they interpret the broader quiet-Sun profiles as due to larger optical thickness. On the other hand, at $T = 80,000$ K, using the corresponding fractional abundance value of Arnaud & Rothenflug (1985), and a photospheric helium abundance of 0.085 (Richard et al. 1998), we estimate, at a hydrogen density of 10^{10} cm^{-3} , that the center-line opacity is of the order of 1 km^{-1} or more (depending on the amount of nonthermal broadening). The opacity is higher by a factor 2–4 at the temperature of maximum fractional abundance of He^+ . It is therefore unlikely that the He II $\lambda 304$ line is optically thin, either in the quiet Sun or in active regions. Our conclusion is consistent with the estimates by CJ75 and MJ99 of $\tau(304 \text{ \AA}) \geq 10$.

If the He II $\lambda 304$ line is optically thick, its width would increase relatively slowly with optical depth. According to the approximate, escape-probability expression of Kastner & Bhatia (1997), the width of an optically thick line increases as $\sqrt{\ln \tau}$. The observed line widths would therefore imply that the optical depths of quiet-Sun profiles are much larger than those in active regions. But line intensities for optically thin or thick lines (but still in the effectively optically thin regime) scale almost linearly with their optical depth (Mihalas 1978, p. 346–349; Jones & Skumanich 1980). Even taking into account a reduction in the collisional source term in the source function, due to the lower density, it is very difficult to obtain a broader but at the same time less intense line in the quiet Sun, compared to active regions. Moreover, both quiet and active profiles are well represented by a Gaussian, while significant differences would be expected if optical depth were the only parameter in determining the difference in line width (see Fig. 2).

If we further assume that the magnetic fields in the radiating features that produce the 304 \AA line have no effect on the line profiles, then the excess broadening in the lower intensity lines cannot be due to optical thickness. This excess residual broadening must then be due to the excess in the actual average nonthermal velocities in the quiet elements over the active elements. This provides us a basis for estimating a lower limit on the actual mean small-scale, nonthermal velocities of the radiating He^+ ions in the quiet Sun.

To do so, we show the intensity and what we have defined as residual line widths in equation (4) and plotted in Figure 3, in the form of scatter-plots, width versus intensity (Fig. 5).

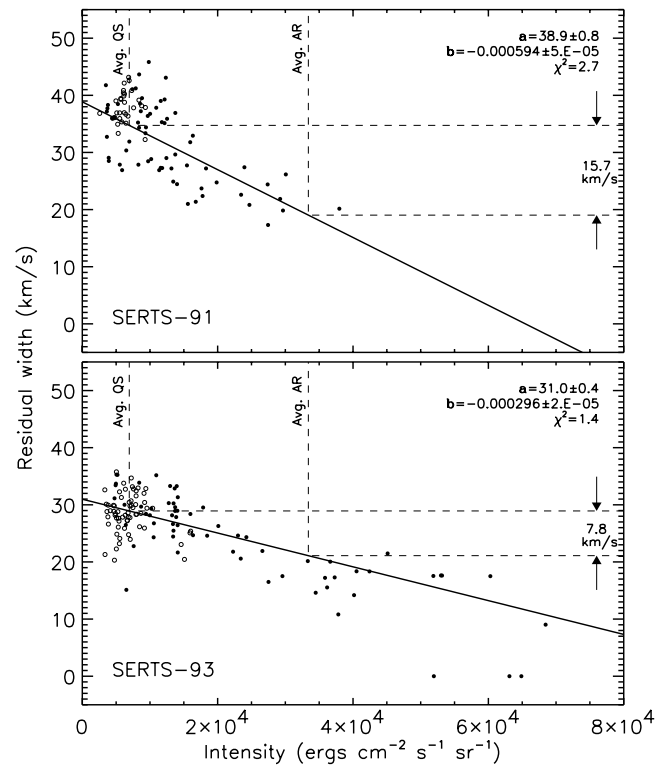


FIG. 5.—Scatter plot of residual line width (W) vs. intensity (I) for SERTS-91 (upper panel) and -93 (lower panel). In both cases, filled-in circles represent data from pointing positions A, while empty circles represent data from positions Q. The parameters of the linear fits to the data, $W = a + b \times I$, are shown in the upper-right corner of each panel, together with their estimated uncertainties and the value of the normalized χ^2 of the fit. On-disk data points for SERTS-91 position Q are displayed, even though they have not been used in the determination of the best-fit line. Estimates for the average increment in nonthermal velocities between quiet and active areas are also shown (see § 2.1.2).

Using the estimated errors on σ_M , and assuming that the uncertainties on σ_I and σ_T are comparatively much smaller, the uncertainties on the residual widths are estimated by propagating the errors in equation (4): $\sigma_R \delta \sigma_R = \sigma_M \delta \sigma_M$. Using these estimates of the uncertainties, $\delta \sigma_R$, we then computed a weighted linear fit to the data.

The three points from SERTS-93 with null residual widths are still shown in Figure 5, even though they have not been used in the fit (their weights would be zero). Moreover, the on-disk points from SERTS-91 position Q are considerably closer to the limb than points from position A or from SERTS-93 (in fact, as described in § 2, at that position the slit crossed the limb). There is therefore the possibility of an additional geometrical effect on the opacity of those line profiles, relative to the observations at position A. We therefore excluded from the fit procedure data from those observations (the corresponding data points are however still displayed in Fig. 5).

From the figure, it is easy to see that both data sets show an anticorrelation between line width and intensity. This result confirms and extends previous reports based on lower spatial resolution observations (Cushman & Rense 1978). However, the fitted correlation from SERTS-91 is to be regarded as less reliable than the correlation from SERTS-93, for two reasons. First, it depends on a smaller number of data points (most quiet-Sun data have been excluded from the fit for the reason given above). And, second, the range of

intensities is smaller (the slit was located only at the periphery of the target active region), and thus does not constrain the anticorrelation as effectively as data from SERTS-93.

If we select the intercept of the fit for SERTS-93 data, in Figure 5, with the two vertical lines to approximate the change in residual line width when going from average quiet-Sun conditions to average active Sun conditions, as determined by the SERTS-93 data analyzed by Brosius et al. (1996), this gives us a measure of the minimum “average” contribution to the residual line width of the actual nonthermal velocity in the quiet elements. The values we obtain for the lower limit, $8\text{--}16\text{ km s}^{-1}$, are also reasonable lower limits for the values obtained from optically thin TR lines around 10^5 K (e.g., Dere & Mason 1993). The actual small-scale velocities of the He^+ ions in these quiet elements could be larger, since we are allowing for the possibility that these velocities are zero in the active elements, and that the higher opacity in the active elements makes no additional contribution to the line widths. This first condition may well be violated and the second one almost certainly is. Thus the values exhibited between the two horizontal lines shown in Figure 5 are certainly a lower limit to the average small-scale nonthermal velocities in the quiet elements.

A clear anticorrelation between line shift and intensity is also present in SERTS-91 data, but it is much weaker in SERTS-93 (see Fig. 3). Analysis of other SERTS data is in progress to further investigate this issue. Moreover, the absolute wavelength calibration of these SERTS spectra is not sufficiently accurate to ascertain whether bright features are redshifted, or it is the fainter features which tend to be blueshifted. The latter case, however, is interesting because it would be consistent with the picture of the velocity redistribution mechanism being more effective in the quiescent atmosphere. In that case, we would expect most of He II emission to come preferably from upward-moving plasma elements (in those atmospheric structures whose temperature gradient is vertically oriented).

3. COORDINATED OBSERVATIONS OF 1998 JUNE

Further tests can be run to assess the region of the quiet Sun most likely to produce the highest enhancement in 304 \AA radiation. In particular, we are interested in locating the regions where most likely the velocity redistribution mechanism is effective, either because of large nonthermal velocities or because of steep temperature gradients. For the latter study, a comparison between network elements and supergranular regions will be indicative. It is interesting that the enhancement factor estimated by MJ99 from an average cell-center spectrum is higher than that estimated from an average network boundary spectrum by about a factor of 2. As noted by those authors, that is consistent with a steeper temperature gradient in cell centers. We will discuss this particular aspect in § 3.2.2.

On the other hand, it is also reasonable to expect an association between enhanced emission in He II $\lambda 304$ and regions associated with the quiet-Sun elements known to have the largest and most complex velocity fields. These regions are found on the boundaries of the supergranulation cells and have been studied extensively in a number of different wavelength positions on the H α line, including the 0.5 \AA red wing (with a 0.2 \AA bandpass) by Beckers (1968), Heinzel & Schmieder (1994), and others. While there is still some ambiguity over what Beckers calls

bright and dark fine mottles and their association with individual spicules and interspicular material, and even some uncertainty on exactly how these disk features rotate onto the limb to correspond to the spicules seen there (Grossmann-Doerth & Schmidt 1992), there is general agreement that the so-called dark coarse mottles seen in the above-noted red wing of H α correspond to the spicule “rosettes” seen on the disk, also called “bushes” as they approach the limb. For illustrations of these observations, the reader is directed to Figure 14 in Beckers and Figure 1 in Heinzel & Schmieder.

We conducted two series of observations to establish the correlation between the He II $\lambda 304$ line emission and the dark coarse mottles observed in the red wing of H α in the quiet Sun. The 304 \AA observations were obtained with the Normal Incidence Spectrograph (NIS) on the *SOHO* Coronal Diagnostic Spectrometer (CDS), and the H α observations were obtained with the solar telescope at the Observatório Astronómico in Coimbra, Portugal. The two series of coordinated observations were taken during 1997 May 7–13 and 1998 June 20–21. In addition to CDS, the first series also featured spectral observations taken with the SUMER instrument on *SOHO*. In exchange for the advantage of the additional high-resolution spectra obtained with the SUMER instrument, it was necessary to conduct the 1997 series near the limb: all the observations were taken at three different solar latitudes, at about $700''$ west of the central meridian. As a result, because of projection effects the correlation between the 304 \AA line and the dark coarse mottles was weaker in that series than in the disk-center observations of 1998 June. We therefore focused on the latter data set.

3.1. CDS Observations

The CDS observations taken during the June 1998 campaign were obtained using an observing sequence identified with the acronym HECATRNW. The normal incidence spectrometer (NIS) of CDS was used with the $4'' \times 240''$ slit. The observing sequence comprises 60 exposures, each one lasting 46 s. After each exposure, the slit is moved by $4''$ east: a complete raster thus covers an area of $240'' \times 240''$ on the Sun. The total duration of the raster is about 54 minutes, including instrumental and telemetry overheads.

The HECATRNW sequence was run nine times on 1998 June 20, starting at 10:01:45 UT, and eight times on June 21, starting at 8:01:55 UT. The pointing of the instrument was chosen to cover an essentially quiet area at the center of the solar disk, as shown in Figure 6.

Because of telemetry limitations, study HECATRNW returns only a portion of the exposed spectra. In the first spectral band (NIS1, $308\text{--}381\text{ \AA}$), four spectral windows are returned; in band NIS2 ($513\text{--}633\text{ \AA}$), 10 spectral windows are returned (three of which overlap to cover a wider wavelength range). The most intense lines in those spectral windows are listed in Table 1. From ionization balance calculations (e.g., Arnaud & Rothenflug 1985), these CDS observations cover solar plasma temperatures ranging from $\approx 2 \times 10^4\text{ K}$ (He I lines) to $\approx 2 \times 10^6\text{ K}$ (Fe XVI line).

Data processing steps (debiasing, cosmic-ray removals, flat-fielding) were performed using standard CDS analysis software. The fit procedures to the line profiles have been performed on the uncalibrated spectrum, which has the advantage of having a nearly constant scattered-light background in both NIS wavelength bands. Atomic data such as

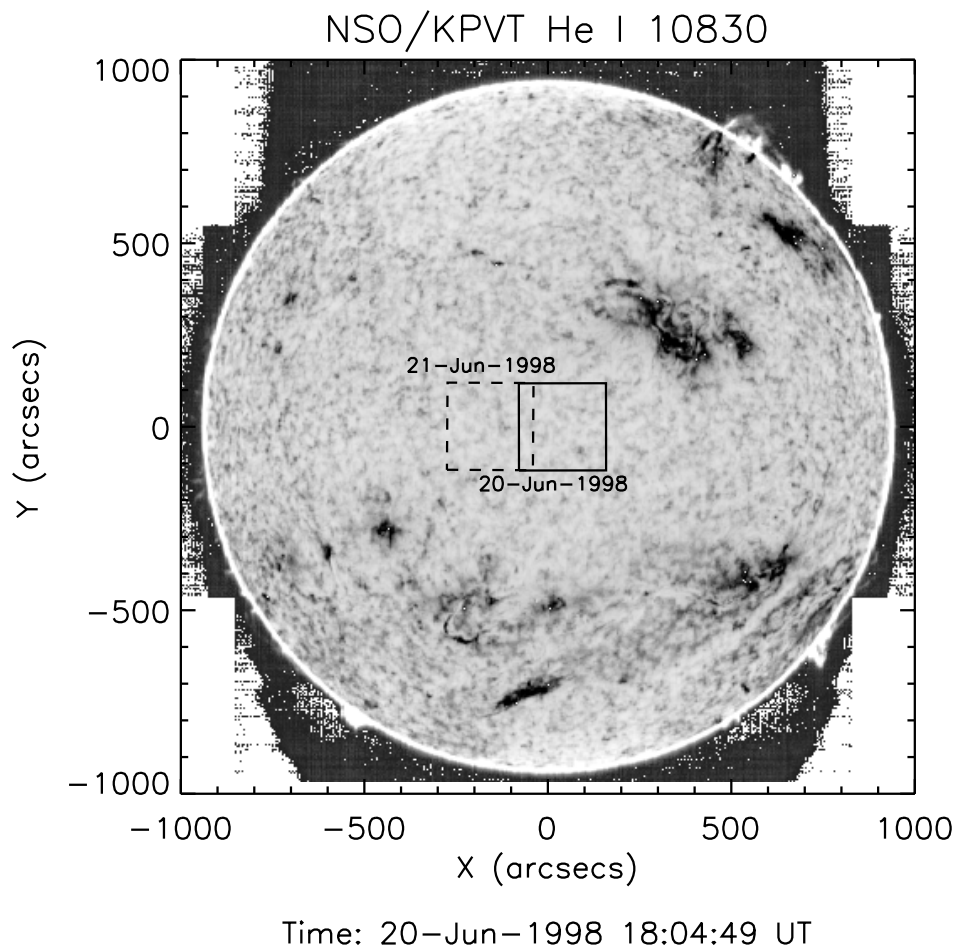


FIG. 6.—Field of view (FOV) for the CDS middle rasters of the series of 1998 June 20 and 21, shown on a synoptic NSO/KPVT He I $\lambda 10830$ image. The FOV coordinates have been rotated to the time of the KPVT image. The active region on the NW of the observed areas is NOAA 8243.

wavelengths or oscillator strengths sometimes necessary in the fits (see below) were mainly derived from the CHIANTI database (Dere et al. 1997). The intensity calibration factors from the CDS analysis software were then applied to the fitted spectra; in particular, we have used the CDS laboratory calibration (Lang et al. 1999) to derive the intensity of

the He II $\lambda 304$ line, which is observed in the second-order spectrum of the NIS wavelength band 2. In this paper we are mainly interested in correlations and relative intensities, thus the accuracy of the absolute intensity calibration is not our prime concern, but it should nevertheless be mentioned that at least two revisions to the “standard” intensity cali-

TABLE 1
LIST OF SPECTRAL WINDOWS OF THE CDS OBSERVING SEQUENCE HECATRNW .

Window	Band	Range (Å)	Lines	log T_{ion}
1+2	2	535.9–540.5	He I $\lambda 537.0$, O II $\lambda 538$, C III $\lambda 538$	4.3, 4.5, 4.85
3+4	2	552.2–556.7	O IV $\lambda 554$	5.2
5	1	346.7–348.1	Si X $\lambda 347.4$	6.1
6	2	583.2–585.5	He I $\lambda 584.3$	4.3
7	1	355.3–356.7	Si X $\lambda 356.0$	6.1
8	2	598.4–600.8	O III $\lambda 599.5$	4.95
9	1	360.1–361.5	Fe XVI $\lambda 360.8$	6.35
10+11	2	605.4–610.1	He II $\lambda 303.8^a$, Si XI $\lambda 303.3^a$, O IV $\lambda 608.4, 609.8$, Mg X $\lambda 609.8$	4.65, 6.2 5.2, 6.05
12	1	367.4–368.8	Mg IX $\lambda 368.1$, Mg VII $\lambda 367.7$	6.0, 5.8
13	2	623.8–626.1	Mg X $\lambda 624.9$	6.05
14	2	628.6–630.9	O V $\lambda 629.7$	5.4

NOTE.—Data taken on 1998 June 20–21. The quantity log T_{ion} refers to the temperature of maximum fractional abundance of the ion, from the ionization balance calculations of Arnaud & Rothenflug 1985.

^a In second-order spectrum.

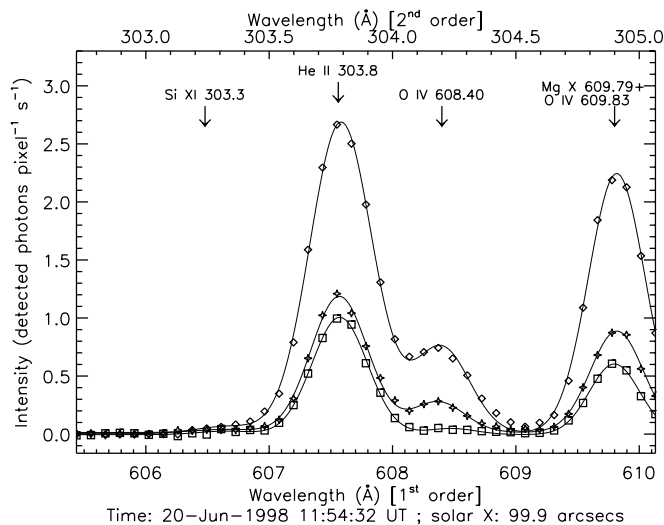


FIG. 7.—Representative CDS/NIS profiles containing the He II $\lambda 304$ line (observed in second order). The spectra shown here are all extracted from the same slit spectrum from the third raster of 1998 June 20 and are therefore simultaneous. Diamonds represent bright network elements; stars represent a spectrum from the boundary of a supergranular cell; squares represent the cell-center spectrum. The solid lines represent multiple Gaussian fits to the spectra.

bration of CDS/NIS have been proposed (Landi et al. 1997; Brekke et al. 2000).

For the present discussion, only the He II $\lambda 304$ and O III $\lambda 600$ lines will be considered in detail. A more complete study of these CDS observations, along with the 1997 May series of observations, will be the subject of a follow-up study. The total intensity of the O III $\lambda 600$ has been determined by fitting each spectrum with a Gaussian profile. The intensity of the He II $\lambda 304$ line required more care because of the proximity of the Si XI $\lambda 303$ line and of other first-order lines.

Figure 7 shows representative intensity profiles from the two overlapping spectral windows covering the wavelength range around the He II $\lambda 304$ line. All the lines indicated in the figure have been fitted with a Gaussian profile. The O IV doublet, arising from the transition $2s2p^2S_{1/2} \rightarrow 2s^22p^2P_{1/2,3/2}$, has been fitted with two Gaussians having the same width, while separation and relative intensity were kept fixed at their theoretical values (1.432 and 1.888 Å, respectively). Of course, the overall wavelength position, total intensity, and line width of the doublet were left as free parameters to fit. Brooks et al. (1999) list an unidentified line at 608.7 Å, which we have not taken into account since it is not likely to have a significant effect on the He II line. Since the Si XI $\lambda 303$ line is normally very weak in our quiet Sun observations, its wavelength and width have also been fixed. This is sufficient to accurately correct its effect on the He II profile.

3.1.1. Co-Alignment of CDS and H α Images

Three H α red-wing spectroheliograms were taken on 1998 June 20, at 11:05, 12:00, and 14:05 UT, while weather conditions did not permit useful observations on June 21. A 0.2 Å bandpass filter set at 0.5 Å from line center was used. In the processing of the data, we have paid particular attention to the issue of the co-alignment of CDS and H α images.

One specific problem stems from the fact that a CDS image is built from a raster lasting almost 1 hr: at the end of

the raster, the location corresponding to the first spectrum has moved west, as a result of solar rotation, by about 8". Consequently, CDS images need to be "destretched" or "differentially rotated": the coordinates of each pixel, that is, should be modified by taking into account the (differential) solar rotation.

Moreover, in the time interval of a CDS raster, there is only one H α available, at most. Thus, besides the obvious problem of comparing features separated in time by as much as half an hour, there is also the problem of choosing the appropriate CDS raster to compare with a given H α image. For example, the east side of the H α image taken at 11:05 UT should be compared with the first CDS raster, which ends at 10:55 UT, while the west side of the images is closer in time to the second CDS raster, which starts at 10:56 UT (the CDS raster mechanism moves the slit from W to E during an area scan, as described in § 3.1).

To partially compensate for this problem, for each H α image we created a CDS "pseudoraster" by first differentially rotating the series of CDS rasters and then by linearly interpolating in time the resulting images at the time of the H α image, on a pixel-by-pixel basis. In this procedure, we adopted the solar differential rotation rate from Howard, Harvey, & Forgach (1990). An example of the result of this procedure is shown in Figure 8. We then coregistered each of these three CDS pseudorasters with the corresponding H α red-wing image by aligning the dark coarse mottles with bright emission in O III $\lambda 600$. The results are illustrated in Figure 9.

3.2. On the Relationship between He II $\lambda 304$ and Chromospheric and TR Structures

We now proceed to the discussion of the tests about the regions of the quiet Sun where the velocity redistribution mechanism is most likely operating. We will examine both the correlation of helium and TR emission with the H α coarse dark mottle structures and the relationship between the He II line and emission in other TR lines, mainly the O III $\lambda 600$ line.

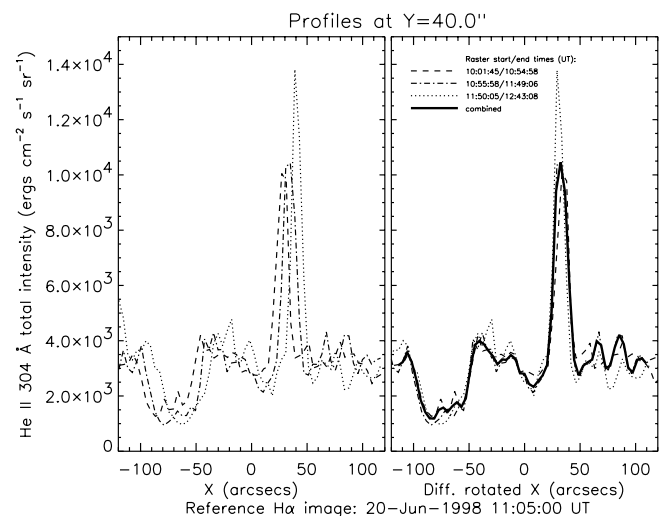


FIG. 8.—Intensity profiles from the three CDS rasters nearest in time to the H α red wing image taken at 11:05 UT on 1998 June 20. *Left panel*: Original data from rasters starting at 10:01:45, 10:55:58, and 11:50:05 UT, coded with dashed, dash-dotted, and dotted lines, respectively. *Right panel*: Differentially rotated profiles, along with intensities interpolated in time to 11:05 UT (thick, solid line).

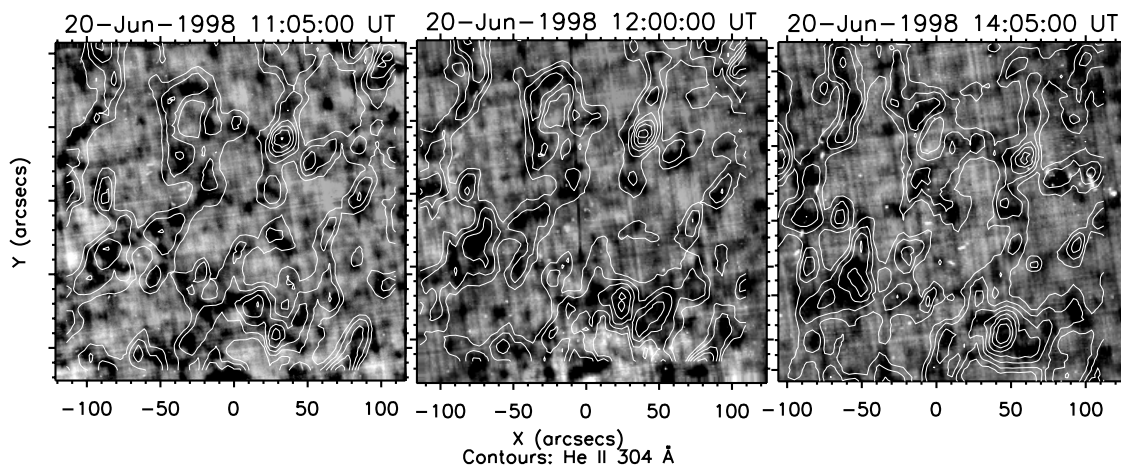


FIG. 9.— $H\alpha$ images of the target quiet area observed on 1998 June 20. Contours of $\text{He II } \lambda 304$ intensity from the “pseudorasters” described in § 3.1.1 are also displayed.

3.2.1. The $\text{He II } \lambda 304$ Line and $H\alpha$ Coarse Dark Mottles

When examining the data taken at Sun center in 1998 June, we found a significant correlation between the $\text{He II } \lambda 304$ line and $H\alpha$ red wing, with correlation coefficients around -0.5 (i.e., bright He II emission tend to correspond to dark $H\alpha$ features). The correlation coefficients between the three $H\alpha$ images of June 20 and the corresponding CDS/NIS pseudorasters created as described in the previous section, are listed in the first column of Table 2.

That helium emission is higher in regions associated with the chromospheric network is not really surprising per se. The signature of the velocity redistribution mechanism would not be an *absolute* intensity enhancement (which even in the standard picture would occur anyway in regions of higher emission measure) but rather a *relative* enhancement with respect to TR line emission. To test this, we chose the O III line at 600 \AA , which is formed under very similar conditions to the 304 \AA line. The correlation coefficients shown in the second column of Table 2 are not significantly different.

Of course, the fact that the O III line correlates equally well with the coarse dark mottle chromospheric structures does not necessarily rule out the velocity redistribution mechanism. It rather suggests a more subtle correlation study, which is reported in the next sections.

3.2.2. A Comparison between the $\text{He II } \lambda 304$ and $\text{O III } \lambda 600$ Lines

The nonthermal velocity field is not the only relevant parameter determining the effectiveness of velocity redistribution: the temperature gradient is an equally important ingredient, as discussed in § 2.1.1. Limiting our attention to quiet-Sun structures, several semiempirical models of the

TR indicate that the temperature gradient in cell centers tends to be higher than in network elements: e.g., Mariska (1992, pp. 169–170) gives a TR temperature gradient from 50% to a factor 3 higher in cell centers (at equal pressures), while MJ99 find a TR thickness that decreases from cell boundaries to interior by a factor ≈ 3 (for equal pressures), or ≈ 40 (using a pressure ≈ 3 times *higher* in cell interiors than in boundaries). For this reason, an analysis of the center-to-boundary behavior of the $\text{He II } \lambda 304$ line is of particular interest.

From the profiles of Figure 7, it is already clear that the intensity of the $\text{He II } \lambda 304$ relative to the $\text{O IV } \lambda 608$ line varies significantly, with the He II line being comparatively more intense in the cell-center profile (although it is fainter there on an absolute scale). Similarly, MJ99 have reported that the ratio $\text{He II } \lambda 304 / \text{O III } \lambda 600$ tends to decrease with the intensity of the latter. This fact is illustrated in Figure 10, for one particular CDS raster. More specifically, the ratio is clearly enhanced toward the supergranular cell interiors. Further, no clear correlation is seen with the coronal $\text{Mg X } \lambda 625$ line, which we might consider as a proxy for the coronal radiation producing the P-R mechanism. A comparison with other TR lines would reproduce essentially the same results. As a summary, the third and fourth columns of Table 2 show the correlation coefficients of the ratio $\text{He II } \lambda 304 / \text{O III } \lambda 600$, which we will denote with R , with both the $H\alpha$ red wing and the $\text{Mg X } \lambda 625$ line, for the three reference pseudorasters.

Because its formation temperature is close to that of the $\text{He II } \lambda 304$, we will once more restrict our attention to the $\text{O III } \lambda 600$ line, whose total intensity we will denote with I_0 . A scatter plot of $\log R$ versus $\log I_0$, in the form of a two-

TABLE 2
VARIOUS CORRELATION COEFFICIENTS DESCRIBED IN §§ 3.2.1, 3.2.2, AND 3.2.3, FOR THE THREE $H\alpha$ RED-WING IMAGES TAKEN ON 1998 JUNE 20 AND THE CORRESPONDING CDS/NIS PSEUDORASTERS

Time	$H\alpha$, He II	$H\alpha$, O III	R , $H\alpha$	R , Mg X	E_R , $H\alpha$	E_R , Mg X
11:05 UT.....	−0.521	−0.545	0.301	0.100	−0.226	0.442
12:00 UT.....	−0.542	−0.552	0.312	0.008	−0.264	0.418
14:05 UT.....	−0.516	−0.522	0.311	0.006	−0.290	0.528
14:05 UT (SW quadrant).....	−0.474	−0.520	0.361	−0.058	−0.276	0.726

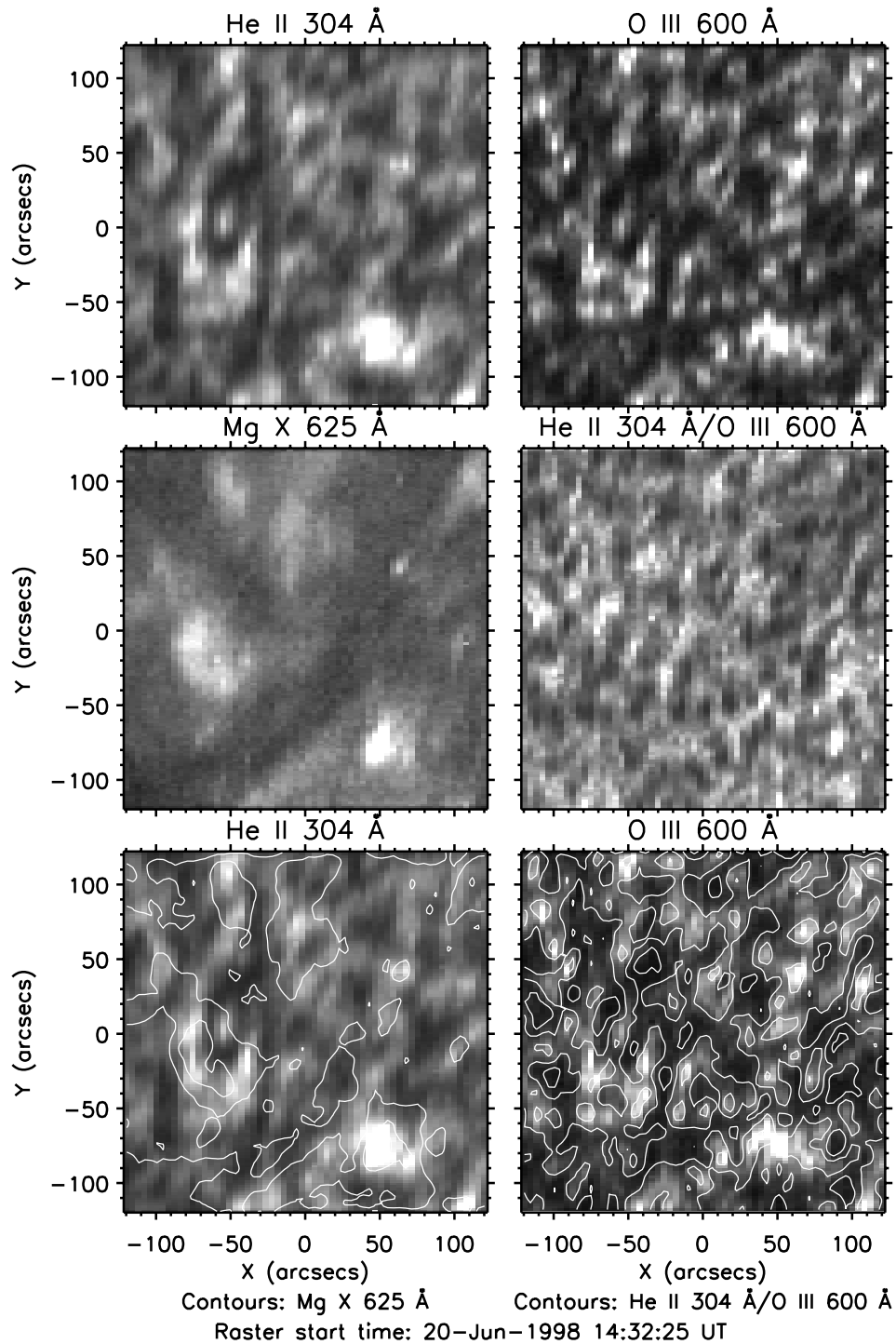


FIG. 10.—Images from a sample raster taken on 1998 June 20, showing a $4' \times 4'$ area at disk center in the He II $\lambda 304$, O III $\lambda 600$, and Mg X $\lambda 625$ lines. The ratio of the He II and O III images is shown in the middle right-hand panel: brighter areas indicate a higher ratio. The same ratio is shown again in the lower right-hand panel as a contour plot overlaid on the O III image. Note the close association of high-ratio areas with dark areas in that line. Finally, the He II and Mg X lines (image and contours, respectively) are compared in the lower left-hand panel.

dimensional histogram (Fig. 11), shows indeed a quite definite anticorrelation between the two quantities. In this case, the correlation coefficient is -0.724 . To construct this two-dimensional histogram, we have used all the data points available for both lines from the 17 rasters taken during the 1998 June campaign. Excluding spectra where line fitting was not possible because of contamination by cosmic rays, we used about 1.36×10^5 spectra, or about 93% of the total.

This two-dimensional histogram can be approximately described by a bivariate normal distribution, with its major axis determined by

$$\log R^{\text{axis}} = 2.740 - 0.510 \log I_0^{\text{axis}}, \quad (17)$$

and with standard deviation in the perpendicular direction $\sigma_{\perp} = 0.0889$ (indicated by a dotted line in the figure). We can use equation (17) as an estimate of the relationship between the He II $\lambda 304$ and O III $\lambda 600$ lines. The logarithmic

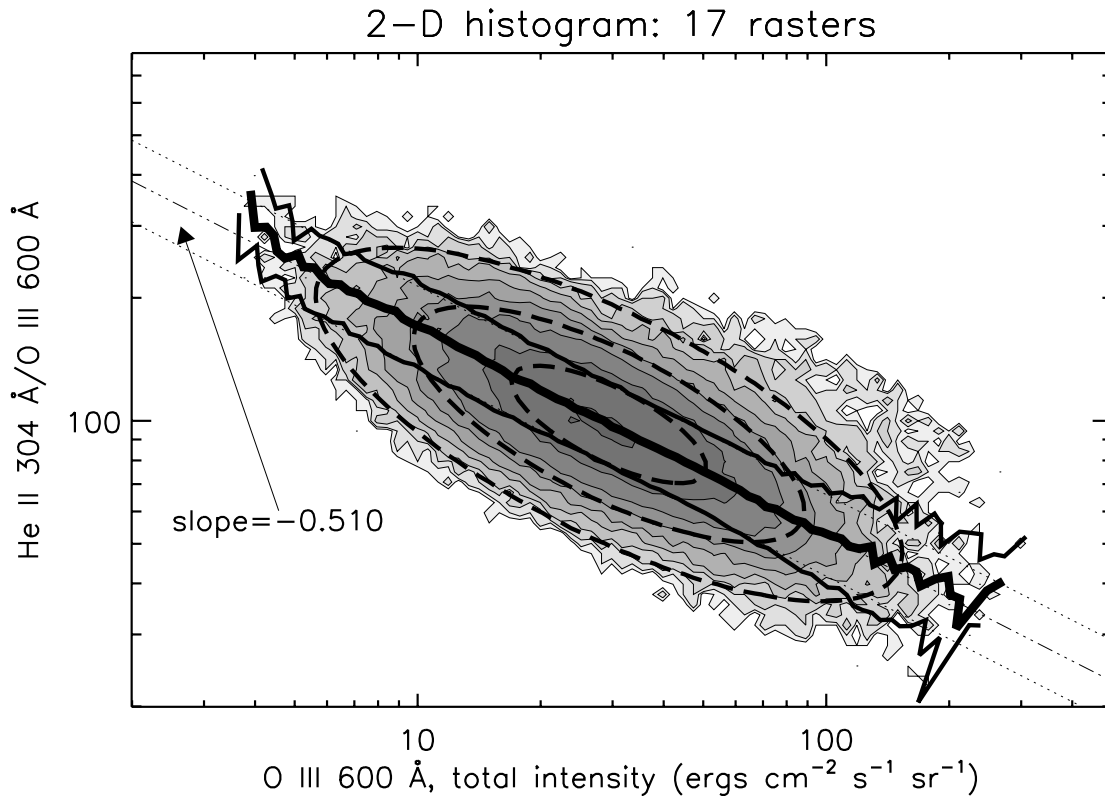


FIG. 11.—Two-dimensional histogram of the ratio R vs. I_0 (see § 3.2.2). Each square bin is of 0.025×0.025 dex. The histogram is represented by filled contours corresponding to 2^n elements per bin, for $n = 0, \dots, 9$. The axis of the bivariate normal distribution fitting the histogram is shown by a solid-dotted line, while the dotted lines represent the width (standard deviation, σ_\perp) of the distribution in the direction perpendicular to the axis. The dashed ellipses represent the 1, 2, and 3 σ contours of the bivariate normal distribution. The average values of the ratio at cross sections of the distribution perpendicular to the axis, spaced by 0.025 dex, are represented by a solid, thick line, while the thinner lines connect the points at $\pm 1 \sigma$.

spacing of the contours in Figure 11 shows that there is a relatively small but significant population of data points well outside of the core bivariate normal distribution, especially at higher values of I_0 . Using other lines, such as the O IV $\lambda 554$ multiplet or the O V $\lambda 630$ line gives similar results but with somewhat smaller correlation coefficients (and slopes). Departures from the bivariate normal distribution also become more pronounced as the difference in formation temperature from the He II $\lambda 304$ line increases.

The intensities of the O III $\lambda 600$ and He II $\lambda 304$ lines, in absence of a significant velocity redistribution effect, are both approximately proportional to the emission measure around $T_e = 10^5$ K, $\mathcal{E} \equiv \int N_e^2 dh$ (where the integration is usually carried out over an interval typically $\Delta \log T_e = 0.1$ or 0.3). Therefore, we can interpret the scatter plot of Figure 11 as an observational plot of the enhancement factor, Y_f , versus emission measure, \mathcal{E} , where $R \sim Y_f$ and $I_0 \sim \mathcal{E}$.

In order to interpret the observed dependence R versus I_0 in terms of the heuristic treatment of the velocity redistribution effect of § 2.1.1, we could introduce scaling laws relating the relevant quantities, V_{NT} , ∇T_e , P_e and \mathcal{E} and then compare the computed variation $Y_f(M)$ (eqs. [15] or [16]) with the observations. From equation (10), and taking into account that the emission measure scales inversely to the temperature gradient, $\mathcal{E} \sim P_e^2 / \nabla T_e$, we have

$$M \sim V_{NT} P_e / \mathcal{E}. \quad (18)$$

As a zero-order approach, we could assume that the observed anticorrelation Y_f versus \mathcal{E} in the quiet Sun is largely due to variations of the temperature gradient, while

variations in pressure and nonthermal velocities are comparatively smaller, on average. Then, using the above relation and the power-law approximation of $Y_f(M)$ with index $p \approx 0.4$ – 0.5 given in § 2.1.1 (see also Fig. 4), we have that over a range of values of M , corresponding to acceptable values for TR temperature gradient, nonthermal velocities and pressures, we would expect

$$Y_f \sim \mathcal{E}^{-p}. \quad (19)$$

We note that the same result would have been obtained under the assumption $V_{NT} P_e \sim \text{constant}$. In any case, it is remarkable that over more than an order of magnitude in intensity, the ratio R has a dependence on I_0 similar, although somewhat steeper, to the dependence of Y_f on \mathcal{E} given by equation (19).

Of course, the model for the velocity redistribution effect described in § 2.1.1 should not be taken too literally. Admittedly, the approximations made to derive the relation of equation (19) from such a model are themselves rather crude. In some respects, the agreement is even surprising. Nevertheless, we think that the evidence presented here is a clue to be seriously taken into account by any more detailed models attempting to describe the empirical properties of the He II $\lambda 304$ line in the quiet Sun.

3.2.3. The He II $\lambda 304$ Line and H α Dark Mottles, Revisited

Figure 11 shows that at higher values of I_0 the ratio R is more likely to be in excess of the value given by equation (17), as discussed in the previous section. We now want to ascertain whether the particularly dynamical regions of the

H α dark mottles could be associated with these anomalous ratios. To do so, we use the information about the width of the two-dimensional distribution R versus I_0 . Given two images in the O III $\lambda 600$ and He II $\lambda 304$ lines, we construct the image ratio, R , and the predicted ratio from equation (17), $R^{\text{axis}}(I_0)$; we then define the “excess ratio”, E_R , as the ratio of the two. The logarithm of E_R is proportional to the distance of the observed value R from the axis of the two-dimensional distribution of ratios.

Figure 12 shows a comparison between such excess ratio derived from two of the CDS pseudorasters and the corresponding H α red-wing images. A comparison with the Mg x $\lambda 625$ images is also shown. There is indeed some association between areas with higher excess ratio and dark mottle structures, but the correspondence is not perfect, in the sense that while higher E_R areas do tend to be associated with dark mottles (with exceptions), not all the H α structures seem to correspond to a particularly high value of E_R . The correlation coefficients summarizing the correspondence E_R versus H α red wing are listed in the fifth column of Table 2. On the other hand, considering the dynamical nature of the H α dark mottles, and that in some regions of the FOV the CDS pseudorasters have been constructed from observations as far as half an hour away from the corresponding H α structures, we can conclude that there is a significant although not one-to-one association with the excess ratio E_R .

However, a comparison with the Mg x $\lambda 625$ line indicates that R is also correlated with coronal structures. This correlation is more clearly definite in bright areas of Mg x emis-

sion. For example, the brightening in the SW quadrant of Figure 12 is closely matched by the area of particularly high values of the excess ratio, E_R . By contrast, the same brightening seen in the CDS raster immediately following the H α image (Fig. 10), has no correlation with the ratio R . This aspect of the relationship with the Mg x $\lambda 625$ line is also seen in the correlation coefficients of the last column of Table 2. In fact, while the correlation between R and the Mg x $\lambda 625$ line is always negligible, there is a significant correlation with E_R . That correlation increases in areas with strong Mg x emission, as shown, for instance, by restricting the correlation analysis to the SW quadrant of the 14:05 UT pseudoraster.

On the basis of this analysis, we may speculate that, while the velocity redistribution is the dominant mechanism for the enhancement of the He II $\lambda 304$ line in the quiet Sun, the P-R mechanism might play a role, although not a dominant one, in areas with brighter coronal emission.

4. DISCUSSION AND SUMMARY OF THE RESULTS

We have exhibited evidence from two instrumentally identical flights of SERTS, in 1991 and 1993, for a strong anticorrelation between total intensity and residual line width in the He II $\lambda 304$ line. We have offered an argument based on these observations and the optically thick properties of this line that establishes an average lower limit on the actual nonthermal velocities of the emitting ions in quiet regions of the Sun. We have also performed some simple model calculations to determine what velocity magnitudes are required for velocity redistribution to contribute signifi-

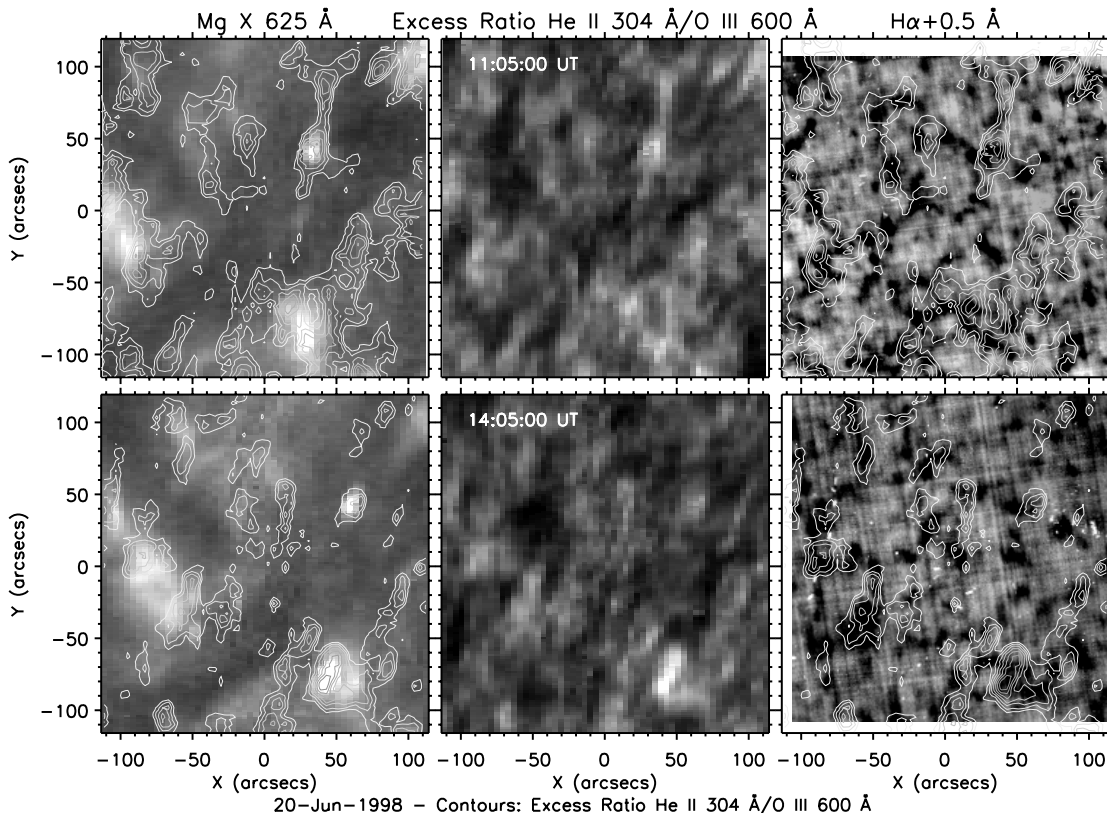


FIG. 12.—Comparison of the “excess ratio” E_R (see § 3.2.3), with two Mg x $\lambda 625$ line (left panels) and the H α red-wing images (right panels). The contours in the outer panels refer to values of E_R corresponding to a distance from the axis of the two-dimensional histogram of Fig. 11 of 0, 0.5, 1, 1.5, 2, 2.5, and $3 \times \sigma_{\perp}$.

cantly to intensity enhancement in the 304 Å line. The velocity magnitudes determined from our He II λ 304 line widths are sufficient to contribute significantly to intensity enhancement but may not be sufficient to explain its magnitude, as estimated by MJ99. We have noted at least one other process, velocity filtration, which may also contribute significantly to the enhancement. On the other hand, the values given for the intensity enhancement of the helium lines in MJ99 could still be revised as the intensity calibration of the *SOHO*/CDS spectrographs is improved.

The empirical anticorrelation of the line width versus intensity we have shown here is a particularly interesting property of the He II λ 304 line requiring further study. Dere & Mason (1993) analyzed the “microturbulent” velocities that were observed with the high resolution rocket telescope and spectrograph. Examining a number of TR lines, including the C IV $\lambda\lambda$ 1548, 1550 and Si IV $\lambda\lambda$ 1393, 1402 doublets as well as other lines forming around the formation temperature of He II λ 304, they inferred microturbulent velocities which appeared to be either constant on average or even to have somewhat higher values in active regions than in the quiet Sun.

One possibility could be that in reality the smaller widths of the He II λ 304 line in active regions are more the result of lower formation temperatures than of smaller nonthermal velocities. That could be a consequence of a possible dominance in active areas of the P-R mechanism, which tends to overionize helium quite deep in the atmosphere (coronal photons below 228 Å are typically completely absorbed or scattered only in the upper chromosphere). The He II line spectrum would therefore form at lower temperatures, and also at much higher line optical depths. But we have shown profiles that, being very close to Gaussians, are hardly compatible with that possibility, unless the spatial scale of our SERTS observations is too large to resolve small active-region radiating elements that produce self-reversed profiles shifted enough in wavelength to “wash out” the central reversal in the observed line. This is an issue we cannot resolve at this time.

On the other hand, Thompson & Brekke (1999) report results from full-disk, spatially averaged CDS observations that seem to indicate a reduction of line width in active regions compared to quiet Sun in He I λ 584, He I λ 522, and O III λ 600 but not in the higher temperature Mg IX λ 368 and Si XII λ 521 lines. Their result regarding the width of TR lines, therefore, seems to be consistent with our findings about the width of the He II λ 304. Moreover, smaller “microturbulent” velocities could well be expected in higher density, active-region plasmas, permeated by stronger magnetic fields. Clearly, this issue merits further investigation both from the observational and the theoretical point of view.

We have also presented a correlation study of the association between H α coarse dark mottles and *SOHO*/CDS spatially resolved observations. When comparing a “typical” TR line, O III λ 600, and the He II λ 304 line, the results are consistent with, but not conclusively in favor of, a dominant velocity redistribution mechanism in the quiet Sun.

The analysis of the ratio He II/O III appeared somewhat more interesting. In particular, we find a qualitative and even semiquantitative agreement (in the sense of scaling laws) between the observed behavior in quiet Sun network structures and what we would expect from the velocity

redistribution mechanism. We also showed that the average observed anticorrelation between that ratio and the intensity of the O III λ 600 line could be interpreted as due mainly to temperature gradient variations.

Moreover, when subtracting the gross, average relationship between the ratio He II/O III and the O III line, obtaining what we call the “excess ratio,” the resulting structures appear to be correlated both with the H α red wing, coarse mottle structures, and with bright coronal emission in Mg X λ 625. We interpreted the latter correlation as an effect of a relatively weak P-R mechanism superimposed on the dominant velocity redistribution process.

While this analysis strongly suggests that velocity redistribution does play a role, alternative explanations for the observed anticorrelation between the ratio He II/O III and the O III line should also be explored. For example, a remaining open question is to what extent the higher He II photon flux in cell center, relative to O III emission, could be explained by resonant scattering of radiation from nearby brighter network structures. In § 2.1.2 we estimated that at densities $N_e = 10^{10} \text{ cm}^{-3}$, the mean free path of a 304 Å photon is only a fraction of a kilometer or less. Nonetheless, multiple resonant scatterings remain a possibility, even taking into account that the vertical stratification of the atmosphere is generally much smaller than the typical distance from the supergranular boundaries to the center of a cell. For a direct verification, this is clearly a problem requiring an adequate treatment of multidimensional, non-LTE radiative transfer. However, we expect that these radiative transfer effects depend on the opacity of the scattering line. Thus, a comparative analysis of the center-to-boundary behavior of lines with very different optical thickness could provide further constraints to the problem.

At this stage it is not possible to say that the problem of the 304 Å intensity enhancement has been solved. What we can say is that there appear to be two candidate possibilities, velocity redistribution and velocity filtration, which are likely to make a significant contribution. The first-named of them is supported by our observations. The P-R mechanism seems to be playing only a secondary role in the quiet Sun. Further constraints can be placed by a more complete analysis of the CDS and SUMER data sets. A detailed examination of the properties of the entire helium spectrum is particularly important because of the several interlocking mechanisms between features of both He I and He II that should be taken into account for a more realistic treatment of the problem (Andretta & Jones 1997).

The follow-up study will also include the use of the high-resolution profiles obtained on the 1997 November 18 SERTS flight for a proper non-LTE analysis of the 304 Å profiles and of other helium spectral features, as these spectra were obtained simultaneously and cospatially with *SOHO*/CDS, and with ground-based H α red-wing images obtained at Coimbra. In addition to the observations already noted, the series of observations taken during 1997 May included nearly simultaneous grazing incidence spectra of the highly ionized iron lines that lie just short of the photoionization limit of He II at 228 Å, using the Grazing Incidence Spectrometer (GIS) on CDS. That will also permit an additional test of the critical hypothesis of electron collisional excitation of the 304 Å in the quiet Sun, using direct observations.

The evidence for collisional excitation of the He II λ 304 line in the quiet Sun is already weighty, and growing, but

the outcome is less certain for active regions, where we plan to extend our analysis. We have reported that nonthermal velocities observed in the region of formation of the He II $\lambda 304$ line seem to be considerably smaller than in the quiet Sun. We have also shown, through an analysis of the He II/O III ratio, that there might be a contribution from the P-R mechanism in bright network elements. Moreover, in the paper by Jordan et al. (1993) a dominance of the P-R mechanism could not be ruled out in active regions. On the other hand, SERTS-97 observations indicate that even in active region, the P-R mechanism is not dominant. We refer to Figure 22 in Swartz et al. (1999), which is a superposition of emission contours in the Fe XVI $\lambda 335$ line onto an emissions map of the 304 Å line observed during the SERTS-97 flight. The Fe XVI line is known to be a good proxy for coronal radiation over a broad wavelength and temperature range (Jordan et al. 1993; Falconer et al. 1998). If P-R were dominating the 304 Å line formation, one would

expect a much closer correspondence between the two different emissions. Yet, the SERTS-97 shows that even in the active region, where our earlier study indicates this P-R process may make some contribution, the correspondence is poor.

This work was carried out while one of the authors (V. A.) held a National Research Council–NASA Research Associateship at Goddard Space Flight Center. V. A. also acknowledges partial funding from NASA/GSFC Grant NCC 5-377. The SERTS program is supported by RTOP grants from the Solar Physics Office of NASA's Space Physics Division. *SOHO* is a project of international cooperation between NASA and ESA. We wish to thank A. K. Bhatia for interesting discussions on some aspects of this paper. We are indebted with the CDS team for their cooperation in planning and carrying out the *SOHO* observations.

REFERENCES

- Aggarwal, K. M. 1993, *ApJS*, 85, 197
 Aggarwal, K. M., Callaway, J., Kingston, A. E., & Unnikrishnan, K. 1992, *ApJS*, 80, 473
 Anderson, S. W. 1994, *ApJ*, 437, 860
 Anderson, S. W., Raymond, J. C., & van Ballegoijen, A. 1996, *ApJ*, 457, 939
 Andretta, V., & Jones, H. P. 1997, *ApJ*, 489, 375
 Arnaud, M., & Rothenflug, R. 1985, *A&AS*, 60, 425
 Athay, R. G. 1988, *ApJ*, 329, 482
 Avrett, E. W. 1999, in Eighth *SOHO* Workshop, Plasma Dynamics and Diagnostics in the Solar Transition Region and Corona (ESA SP-446; Noordwijk: ESA), 141
 Beckers, J. M. 1968, *Sol. Phys.*, 3, 367
 Brekke, P., Thompson, W. T., Woods, T. N., & Eparvier, F. G. 2000, *ApJ*, in press
 Brooks, D. H., et al. 1999, *A&A*, 347, 277
 Brosius, J. W., Davila, J. M., Thomas, R. J., & Monsignori-Fossi, B. C. 1996, *ApJS*, 106, 143
 Cushman, G. W., & Rense, W. A. 1978, *Sol. Phys.*, 58, 299
 Dere, K. P., Landi, E., Mason, H. E., & Monsignori-Fossi, B. C. 1997, *A&AS*, 125, 149
 Dere, K. P., & Mason, H. E. 1993, *Sol. Phys.*, 144, 217
 Falconer, D. A., Jordan, S. D., Brosius, J. W., Davila, J. M., Thomas, R. J., Andretta, V., & Hara, H. 1998, *Sol. Phys.*, 180, 179
 Fontenla, J. M., Avrett, E. H., & Loeser, R. 1993, *ApJ*, 406, 319
 Grossmann-Doerth, U., & Schmidt, W. 1992, *A&A*, 264, 236
 Heinzel, P., & Schmieder, B. 1994, *A&A*, 282, 939
 Howard, R. F., Harvey, J. W., & Forgach, S. 1990, *Sol. Phys.*, 130, 295
 Jones, H. P., & Skumanich, A. 1980, *ApJS*, 42, 221
 Jordan, C. 1975, *MNRAS*, 170, 429
 ———. 1980, *Philos. Trans. R. Soc. London*, A297, 541
 Jordan, S. D. 1994, *IAU Colloq.* 144, Solar Coronal Structures, ed. V. Rušin, P. Heinzel, & J.-C. Vial (Tatranská Lomnica: Veda), 415
 Jordan, S. D., Thompson, W. T., Thomas, R. J., & Neupert, W. M. 1993, *ApJ*, 406, 346
 Kastner, S. O., & Bhatia, A. K. 1997, *J. Quant. Spectrosc. Radiat. Transfer*, 58, 217
 ———. 1998, *MNRAS*, 298, 763
 Kohl, J. L. 1977, *ApJ*, 211, 958
 Landi, E., Landini, M., Pike, C. D., & Mason, H. 1997, *Sol. Phys.*, 175, 553
 Lang, J., et al. 1999, The Laboratory Calibration of the *SOHO* Coronal Diagnostic Spectrometer, technical report, RAL-TR-1999-036, Rutherford Appleton Laboratory
 Macpherson, K. P., & Jordan, C. 1999, *MNRAS*, 308, 510
 Mihalas, D. 1978, *Stellar Atmospheres* (2d ed.; San Francisco: Freeman)
 Mariska, J. T. 1992, *The Solar Transition Region* (Cambridge: Cambridge Univ. Press)
 Milkey, R. W. 1975, *ApJ*, 199, L131
 Neupert, W. M., Epstein, G. L., Thomas, R. J., & Thompson, W. T. 1992, *Sol. Phys.*, 137, 87
 Raymond, J. C., & Doyle, J. G. 1981, *ApJ*, 247, 686
 Richard, O., Dziembowski, W. A., Sienkiewicz, R., & Goode, P. R. 1998, *A&A*, 338, 756
 Scudder, J. D. 1992a, *ApJ*, 389, 319
 ———. 1992b, *ApJ*, 266, 339
 Shine, R. A., Gerola, H., & Linsky, J. L. 1975, *ApJ*, 202, L101
 Swartz, M., et al. 1999, The SERTS-97 Rocket Experiment to Study Activity on the Sun: Flight 36.167-GS on 1997 November 18 (NASA/TP-1999-208640; Goddard Space Flight Center: NASA)
 Thompson, W. T., & Brekke, P. 1999, *Sol. Phys.*, in press
 Viñas, A. F., Wong, H. K., & Klimas, A. J. 2000, *ApJ*, 528, 509
 Zirin, H. 1988, *Astrophysics of the Sun* (Cambridge: Cambridge Univ. Press)